Soil Dynamics and Earthquake Engineering 157 (2022) 107247

Contents lists available at ScienceDirect

Soil Dynamics and Earthquake Engineering

journal homepage: www.elsevier.com/locate/soildyn

# Statistical distributions of wave velocities and elastic moduli in near-surface unsaturated soils

Oliver-Denzil S. Taylor [a,*], Masood Abdollahi [b], Farshid Vahedifard [b]

[a] U.S. Army Engineer Research and Development Center (ERDC), Geotechnical and Structures Laboratory, Vicksburg, MS, 39180, USA
[b] Richard A. Rula School of Civil and Environmental Engineering, Mississippi State University, Mississippi State, MS, 39762, USA

ARTICLE INFO

*Keywords:*
Unsaturated soils
Statistical distribution
S-wave velocity
P-wave velocity
Elastic moduli
Variability Poisson's ratio

ABSTRACT

The shear wave velocity ($v_s$) and the compressional wave velocity ($v_p$) are extensively used to understand the near-surface geologic structure, derive small-strain elastic moduli of soils, and perform a wide range of geophysical, geotechnical, and geo-environmental analyses. While the dependency of $v_s$ and $v_p$ on water content or degree of saturation is well recognized, the variability of wave velocity measurements and derived elastic moduli within different saturation levels remains yet to be understood. The main objective of this study is to examine the effect of degree of saturation on the statistical distribution of measured wave velocities and the derived small-strain elastic moduli in unsaturated soils. For this purpose, 360 ultrasonic laboratory tests, an extensive array, were performed on a poorly graded fine-to-medium sand over seven full wetting-drying cycles. The laboratory-measured data were used, along with a suite of statistical tests, to evaluate the statistical distribution and variability of the $v_p$ and $v_s$ measurements and the derived elastic variables–including $v_p/v_s$ ratio, shear modulus ($G$), Young's modulus ($E$), Poisson's ratio ($\mu$), and bulk modulus ($K$). The results show that many of the assumptions regarding the quantification of $v_p$ and $v_s$ measurements and elastic moduli used in geophysical, geotechnical, and geo-environmental analyses may not be valid. The $v_p$ and $v_s$ data are best represented by lognormal and Weibull distributions, respectively, yet the subsequently derived elastic properties may require more than one distribution type to adequately represent the statistical behavior for different saturation regimes and relationships.

## 1. Introduction

The shear wave velocity ($v_s$) and the compressional wave velocity ($v_p$) measurements from the field or laboratory are widely used in a variety of subsurface and near-surface geophysical applications (see Supporting Information for details). These wave velocity measurements can be employed to investigate events of interest, such as discrimination of nuclear and chemical explosions [1], pipeline explosions [2], high-resolution seismic refraction tomography [3–6], hydro-mechanical soil behavioral investigations [7–9], environmental monitoring [10,11], and military events [12]. Furthermore, $v_s$, $v_p$, and the $v_p/v_s$ ratio are of critical importance to understand the near-surface geologic structure and the derivation of small-strain elastic moduli [13–18]. For instance, $v_s$ is commonly employed to estimate the condition of shallow soils and analyze their seismic response, susceptibility to liquefaction, and other geophysical and geotechnical earthquake engineering applications [19].

Among other factors, water content or degree of saturation is recognized to have a notable effect on $v_s$ and $v_p$ measurements. Changes in degree of saturation vary interparticle contacts and water phase, both of which affect the wave propagation speed thorough porous media, causing the dependency of $v_s$ and $v_p$ on degree of saturation. While several experimental studies have shown that $v_p$ increases upon saturation [16,20–24], a second group of studies have reported a contradictory trend using laboratory test results [1,15,25–29]. These opposing trends can be possibly attributed to variations in confining pressure, initial conditions, hydraulic conductivity, and soil type used in these studies [18]. On the other hand, there is a consensus in the literature that $v_s$ decreases upon saturation [15,22,29,30]. The influence of degree of saturation on $v_s$ can be interpreted through its impact on the soil effective stress [18]. This effect is more pronounced in soils having fine particles such as silt or clay [31]. For example, [26], showed that $v_s$ in compacted clay could increase from 300 m/s to 800 m/s as matric suction increased from 300 kPa to 15,000 kPa.

While the effect of degree of saturation on $v_s$ and $v_p$ is well studied in

* Corresponding author.
*E-mail addresses:* oliver.d.taylor@usace.army.mil (O.-D.S. Taylor), ma1882@msstate.edu (M. Abdollahi), farshid@cee.msstate.edu (F. Vahedifard).

https://doi.org/10.1016/j.soildyn.2022.107247
Received 15 October 2021; Received in revised form 18 February 2022; Accepted 9 March 2022
0267-7261/Published by Elsevier Ltd.

the literature, limited, if any, studies have been performed to characterize the variability of wave velocity measurements and derived elastic moduli within different saturation levels. In exploration geophysics, the impacts of meteorological events (e.g., the influx of water into the soil structure) may not readily correlate with the recorded data or the empirically derived mean characteristic soil property (e.g., $v_p$ and $v_s$ measurements and elastic moduli). Subsequent signal processing and data analysis do not account for this variability caused by the dynamic effects associated with changes in matric suction [16,32,33]. Beyond geophysical research, considering the variability of unsaturated soil properties is of great importance in engineering analyses of unsaturated slopes and earthen structures [33–37] and environmental evaluation procedures [10,11]. Most of the existing studies have attributed the variability of unsaturated soil properties to the uncertainty associated with the soil water retention curve (SWRC) [33,38–41]. However, several of these analyses (e.g., seismic hazard calculations, site response analyses, and soil–structure interaction problem) heavily rely on and directly employ geophysical measurements or estimations of $v_p$ and $v_s$ and the derivation of elastic moduli. Thus, $v_p$- and $v_s$-saturation relationships and their subsequent distributions are one of the most important sources of uncertainty in engineering applications, and quantifying the respective variabilities is a vital step in evaluating the accuracy of geotechnical designs and geophysical analyses [16,38,42].

To address the aforementioned gaps, the main objective of this study is to investigate the following: (a) the assumption that the derived elastic moduli are constant or only density variable within the unsaturated regime, (b) the effect of the unsaturated regime on the statistical distribution of measured $v_p$- and $v_s$-saturation relationships, which determine the experimental mean used in geophysical and geotechnical analyses, and (c) the potential change in statistical distribution types within elastically derived small-strain elastic moduli in unsaturated soils. For this purpose, 360 ultrasonic laboratory tests, an extensive suite, was performed on a washed, poorly graded, fine-to-medium quartz-silica beach sand over seven full wetting-drying cycles to establish a statistically relevant dataset to investigate statistical properties about a best-fit regression mean. The laboratory-measured data were then used, along with a suite of statistical analyses, to evaluate the statistical distribution and variability of the $v_p$ and $v_s$ measurements and the derived variables.

## 2. Background

For an elastic, isotropic, and homogeneous soil, one can employ the elastic theory to establish the following relationships:

$$G = \frac{\gamma v_s^2}{g} \tag{1}$$

$$\mu = \frac{\left(v_p/v_s\right)^2 - 2}{2\left(v_p/v_s\right)^2 - 2} \tag{2}$$

$$E = 2G(1+\mu) \tag{3}$$

$$K = G\left[\left(\frac{v_p}{v_s}\right)^2 - \frac{4}{3}\right] \tag{4}$$

where $G$ is shear modulus, $\gamma$ is the unit weight of the media, $g$ is the gravitational acceleration, $\mu$ is Poisson's ratio, $E$ represents Young's modulus, and $K$ denotes bulk modulus.

There are two distinct areas associated with variability and uncertainties in determining wave velocities and small-strain elastic moduli: (a) the assumption of discrete or constant distributed small-strain elastic moduli and (b) the epistemic uncertainty in the laboratory determination of wave arrival times. Both of these sources of uncertainty are amplified under low-confinement and unsaturated conditions [16,32]. The discrete value obtained from the elastic approximation is often assumed a mean quantity, but little is known about the statistical properties of this value (e.g., the distribution type, skewness, and kurtosis). In cases where experimental data are available, a fit through a minimum least-squares regression, often about the mean or median of the data set, will define measured parameters, (i.e., $v_s$ and $v_p$ [43]). Provided a high "goodness" of fit ($R^2 \geq 0.75$), such a regression can illustrate a behavioral trend though it does not provide insights into the statistical distribution of the data about. The distribution of data about the best-fit regression, taken as the mean of the data, is critical for probabilistic analysis of characteristic soil properties used for engineering design [38,44–46]. Typically, a distribution type, e.g., normal, lognormal, gamma, etc., is assumed as representative of the totality of the elastic properties. That is, if a lognormal distribution is determined as the best-fit of the $v_s$ data, the same distribution type (lognormal) is then assumed for other elastic moduli derived from $v_s$. In theory, if the material adheres to elastic continuum behavior this assumption should hold true wherein the inherent variability should remain constant, i.e., there should not be a change to the data distribution due to the mathematical relationships. In this study, we aim to test this hypothesis through an extensive set of laboratory-measured data.

## 3. Experimental setup and testing procedure

### 3.1. Tested material

The testing program was performed on a washed, poorly graded, fine-to-medium quartz-silica beach sand with 90% of the particles between 0.25 and 0.85 mm in diameter. The coefficient of uniformity ($c_u$) and coefficient of curvature ($c_c$) of the grain-size distribution are 1.52 and 1.12, respectively. The specific gravity is ($G_s$) 2.67. Samples were reconstituted, using the [47] protocol at a reconstituted saturation of 24% and a compaction energy of 600 kJ/m$^3$ (E600), samples were reconstituted into a soil fabric comparable to the in situ field conditions observed by Ref. [32]. This method was employed to prepare the samples in a highly repeatable manner with uniform densities, moisture contents and soil fabric throughout the specimen. Moreover, this method significantly reduces the epistemic uncertainty within testing results and generates a repeatable reconstituted soil fabric across multiple specimen configurations and testing apparatuses allowing for a direct correlation in the experimental data and results. Fig. 1 depicts the SWRC of the tested soil [data from Ref. [33] and [48]].

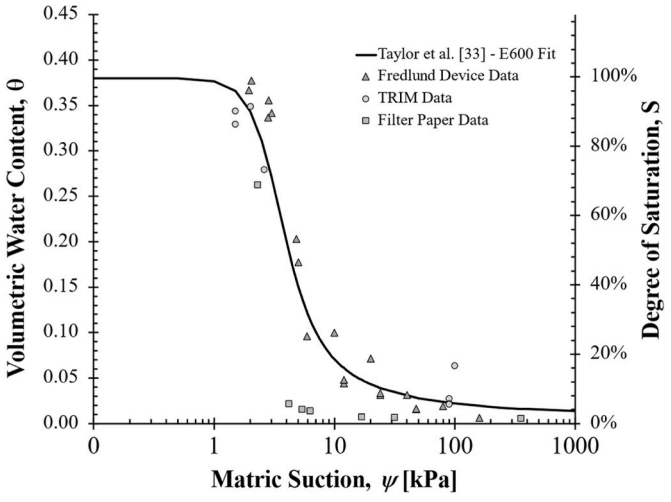


**Fig. 1.** The soil-water retention curve, SWRC, for the tested soil [data from [33] and [48]].

### 3.2. Test apparatus

In this study, we used the Ultrasonic Near-Surface Inundation Testing (UNIT) device, developed by the U.S. Army Engineer Research and Development Center (ERDC) [16,49,50], to measure $v_s$ and $v_p$. The UNIT, Fig. 2, is a cubic acrylic chamber, 15 × 15 × 15-cm interior dimension, an atmospheric free-surface top plate, and horizontal bender element ports to measure seismic wave propagation perpendicular to the direction of fluid infiltration. An atmospheric, elastic, free surface air/soil interface allows for the development of uninhibited soil swell characteristics and is essential for near-surface investigations. Furthermore, the shape, materials, and size of the device ensure that wave reflectance and the artificial transmission of the source signal around the outside of the cell chamber are effectively eliminated. All water used within the UNIT device is purified, distilled, and de-aired to remove the potential of chemical contaminants that could introduce an artificial bonding of soil particles.

The UNIT device uses piezoelectric bender elements to measure $v_s$ and $v_p$. The bender elements consist of a paired piezoelectric $v_p$ and $v_s$ transducers that are of variable excitation frequency (excitation frequencies of 10-, 14- and 20 kHz are used in this data), 14-V sine wave drivers. The bender element source and receiver are orientated in parallel to measure the radial wave motion associated with $v_p$ and $v_s$ waves. A series of moisture sensors are used to confirm the degree of saturation and two piezometers are stacked vertically on the side of the sample chamber opposite moisture sensors to measure fluid pressures above and below the horizontal propagation pathway to ensure saturation equilibrium. It is noted that a high degree of uncertainty within historical data can be traced to the method of interpretation used to determine wave travel times, and this uncertainty is compounded through the calculations of elastic moduli. Seismic sources were generated as 10-, 14-, and 20 kHz sine waves yielding a $\lambda/lb \leq 4$, which may allow for the use of the peak cross-correlation between the input and output signals to quantify an accurate $v_s$ travel time. The $v_p$ was excluded from the cross-correlation analysis by identifying the end of the $v_p$ in the time-series, and only performing the cross-correlation for the remaining time history. However, recent research has noted that with a decrease in $v_s$ amplitude with saturation can lead to erroneous the cross-correlation arrival time detection even though the $v_s$ arrival can be visually identified; indicative of significant changes to wave energy and spectral content [16,50]. Within the results of [16,50] and those presented herein, there was no correlatable data with respect to a cross-correlation acceptability-saturation relationship to define when or at what statistical frequency cross-correlation methods would yield erroneous arrival times. Therefore, determination of the $v_s$ arrival time through the convergence of numerical cross correlation and manual inspections was carried out for all $v_s$ data. All $v_p$ data was determined through visual inspections by multiple researchers of both the $v_p$ source bender elements and from the side lobes generated $v_p$ from the corresponding s-wave bender elements to reduce any implicit bias in arrival time determination. It must be noted that only $v_p$ bender element generated data is presented herein.

[16] showed that for near-surface sands under low confining pressures, the uncertainties associated with laboratory experimentation could be significantly reduced through (a) a rigorous energy-controlled sample preparation technique, (b) the use of the UNIT device, (c) determination of the $v_s$ arrival time through the convergence of numerical cross correlation and manual inspections, and (d) determination of the $v_p$ arrival time through manual inspection of a truncated time-series. We applied all of the aforementioned factors to minimize the uncertainties associated with laboratory experimentation and determination of wave arrivals.

### 3.3. Testing procedure

The UNIT device measures the ultra-low confining pressure $v_s$- and $v_p$-saturation relationships via piezoelectric bender elements with arrival times determined by the convergence of (1) manual inspection and (2) cross correlation [49,50]. The $v_s$ and $v_p$ time histories are composed of a minimum of 50 stacked waveforms to determine the correct convergence and wave travel times (Fig. 3). In the determination of $v_s$, the $v_p$ time-history was excluded from the cross correlation by identifying the end of the $v_p$ time-series and performing the cross correlation on the signal only after that time [16,49]. Once the $v_s$ and $v_p$ data were obtained, the elastic moduli were calculated based on Eqs. (1)–(4).

To investigate the $v_s$- and $v_p$-saturation relationships at discrete controlled saturation intervals and eliminate hydraulic flow forces, no flow was allowed through the specimen (the UNIT drainage valve was set to an impervious condition). Saturation was achieved by pipetting 70 mL of water uniformly to the top surface of the specimen over a 5-min period. The specimen was then covered with plastic wrap to prevent evaporation, and allowed to reach a hydraulic equilibrium, determined by no additional change in the pore pressure transducers: this process takes 4 h for the study material. After hydraulic equilibrium is achieved, $v_s$- and $v_p$ measurements are recorded and stacked at the known degree of saturation. This process was repeated until no further absorption of the pipetted water is observed and hydraulic equilibrium within the pore pressure sensors is maintained; defining the maximum saturation potential of the soil without the application of external pressures. Once the specimen achieved maximum saturation, the specimen was allowed to dry while continuing to take moisture and wave speed measurements at discrete drying time intervals. A single wetting-drying cycle was conducted over a 3-month timeframe under controlled ambient conditions: 21 °C at a relative humidity between 55 and 60%.

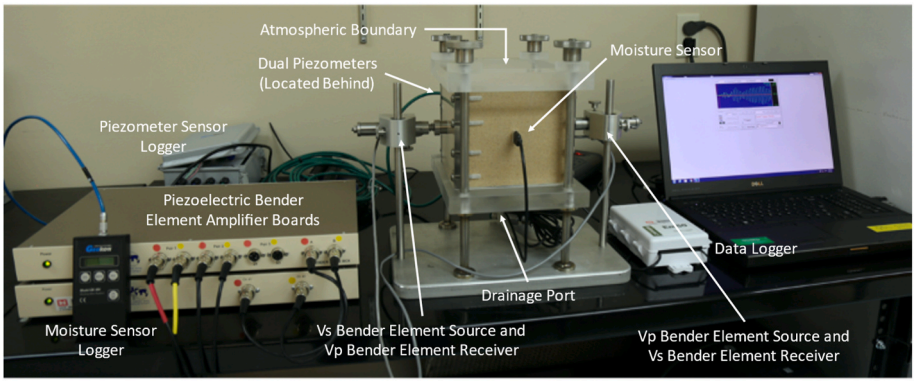


**Fig. 2.** The Ultrasonic Near-Surface Inundation Testing (UNIT) device used in this study.

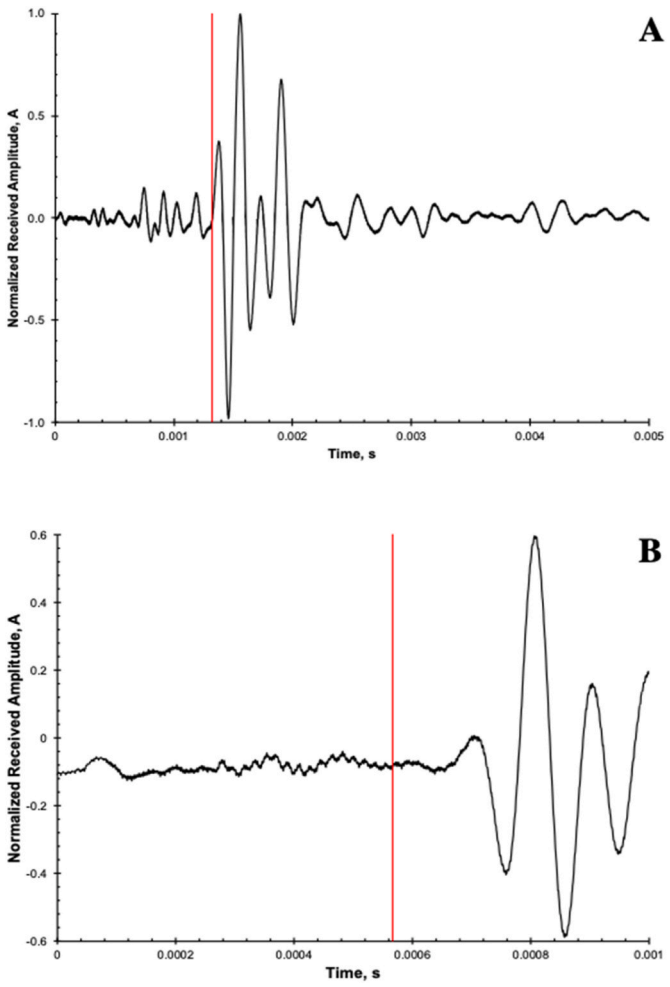


**Fig. 3.** Determination of wave arrival times from a minimum of 50 stacked waveforms: (**A**) $v_s$, and (**B**) $v_p$ waveforms. Red lines indicate the convergence arrival time from cross-correlation and manual determinations.

## 4. Experimental results

Building upon the experimental data in Ref. [16], a total of 262 $v_s$ data were measured based on the arrival time histories of a minimum of 50 stacked ultrasonic waveforms over 7 full wetting-drying cycles (Fig. 4a). The $v_s$ source excitation frequency was varied, beyond the standard 10-kHz excitation frequency, in three of these cycles (to 14-, and 20-kHz) to ensure frequency independence within the data and that the ratio of the transmitted signal wavelength to the bender element's wavelength does not impact the accuracy of the stacked time histories. As seen in Fig. 4a, there is no observable or discernible wetting-drying hysteretic behavior for this material over the totality of the evaluated wetting-drying cycles; a similar observation is shown by Ref. [16]. Rather, the inherent experimental scatter, for given degree of saturation, is attributed to the summation of aleatory variability and epistemic uncertainty.

Fig. 4b depicts the results of 98 $v_p$ measurements, which are derived from a minimum of 50 stacked ultrasonic waveforms and correspond to 5 wetting-drying cycles. Based on the $v_s$ measurements, it is assumed that the excitation frequency independence exists within the data, thus only the 10-kHz excitation frequency is used in the $v_p$ measurements. Observationally, no hysteretic wetting-drying behavior is identifiable over multiple wetting-drying cycles on the same UNIT specimen. Therefore, drying and wetting cycles are treated equally, in terms of quantifying $v_p$-saturation relationships and statistical variability.

## 5. Statistical analyses and discussion

In this study, we used R-Studio-1.4.1106, R [51], to statistically evaluate the measured data, Fig. 4 and the derived moduli, Fig. 5. The distribution fitting package "Fitdistrplus" is employed to find the best distribution for the range of data presented in this study. Fitting distributions to data is a common practice in statistics and includes choosing a probability distribution function of a random variable that best fits a set of data, as well as finding parameter estimates for that distribution. In this study, the distribution parameters are estimated by maximizing the likelihood function using the optimum function. In the R [51] package MASS [52], maximum likelihood estimation is available via the "fitdistr" command. Choices of best fit and goodness of different types of distributions are then investigated through goodness of fit plots [53].

The Cullen and Frey [53] Graph, (CFG) also known as the skewness-kurtosis graph, was used to identify the choice of a best fit for

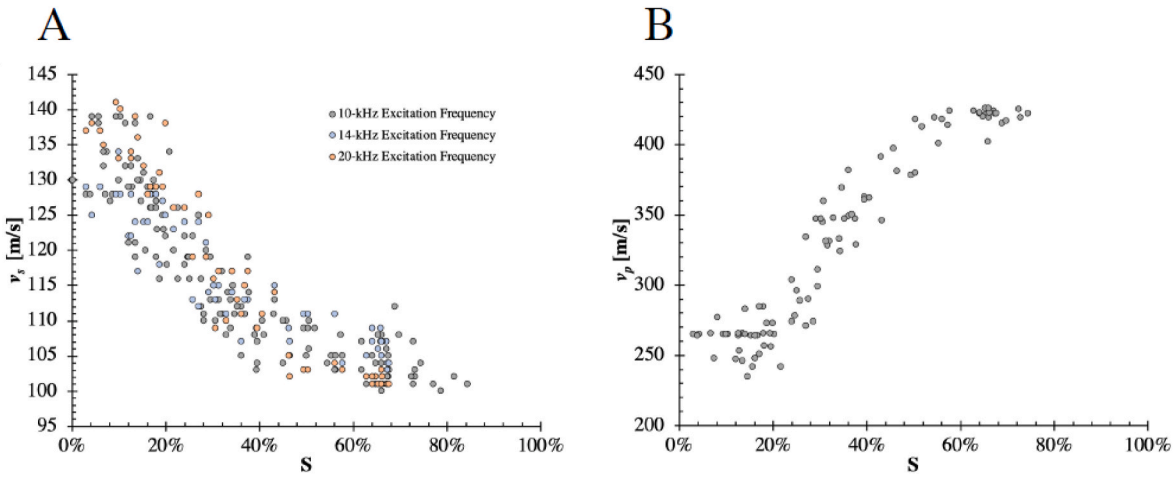


**Fig. 4.** (**A**) Measurements of $v_s$ versus degree of saturation based on the stacked arrival time histories (mean of 52 stacked waveforms per data point) at different excitation frequencies. Grey circles are 10-kHz excitations over 7 full wetting-drying cycles (149 data points); blue circles are 14-kHz excitation frequencies over 3 full wetting-drying cycles (57 data points); and orange circles are 20-kHz excitation frequencies over 3 full wetting-drying cycles (56 data points); (**B**) Measurements of $v_p$ versus degree of saturation based on the stacked arrival time histories (10-kHz bender element excitation frequency with a mean of 52 stacked waveforms per data point, total of 98 points).

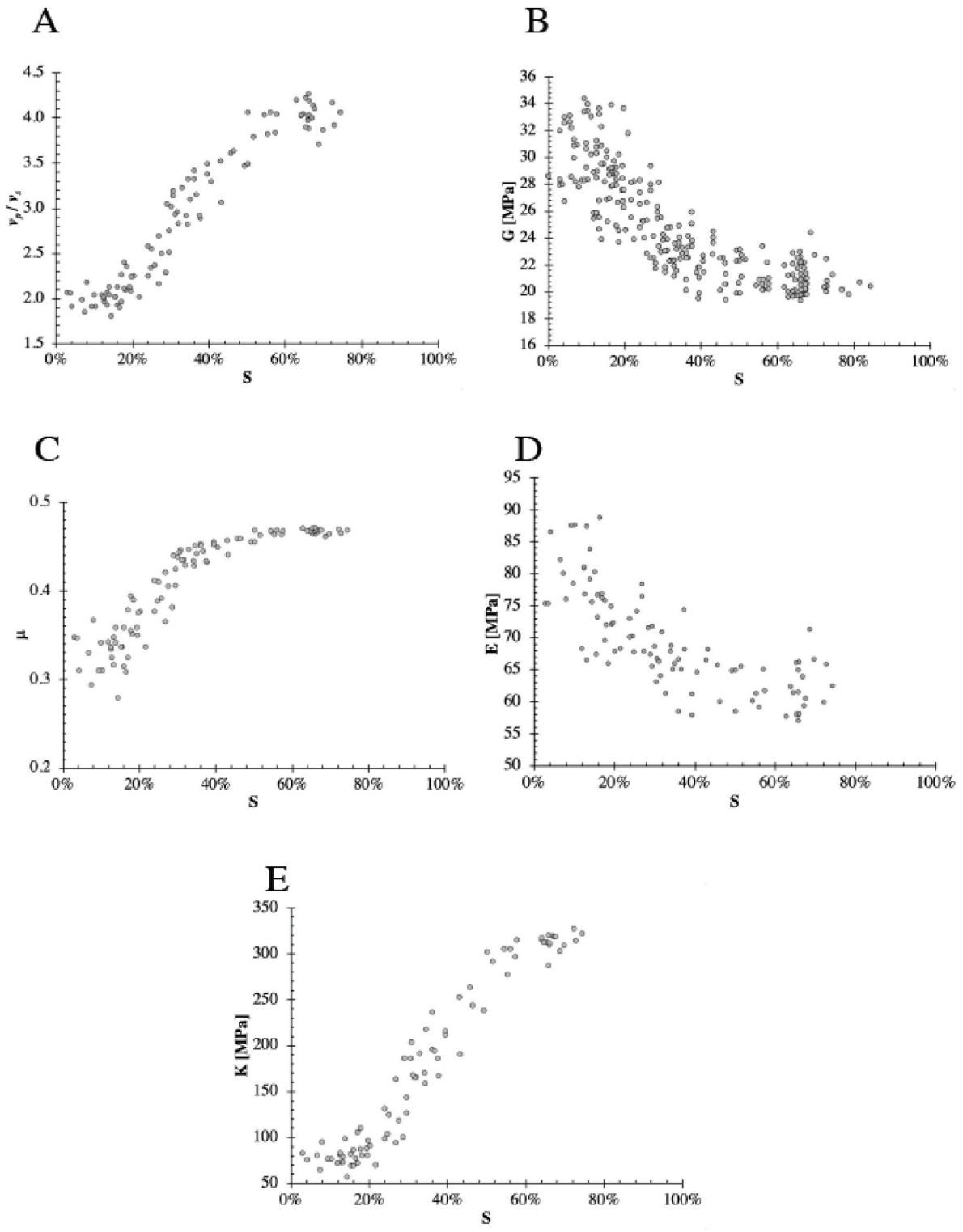


**Fig. 5.** (**A**) $v_p/v_s$ ratio for the correlated $v_p$ and $v_s$ measurements (no. of data points: 98); (**B**) derived values of G versus degree of saturation, S, from Eq. (1) (no. of data points: 262); (**C**) derived values of $\mu$ versus S from Eq. (2) (no. of data points: 98); (**D**) derived values of E versus S from Eq. (3) (no. of data points: 98); (**E**) derived K versus S from Eq. (4) (no. of data points: 98).

an unknown distribution according to skewness and kurtosis of data. Kurtosis is a measure of tailedness of the probability distribution wherein a value less than 3 indicates the distribution produces fewer outliers than does the normal distribution. The Cullen and Frey graph uses predefined distributions (e.g., normal, lognormal, Weibull) to perform moment or maximum likelihood fitting. The x-axis represents the square of skewness and the y-axis is kurtosis. If the skewness and kurtosis of the observation data are similar to those of a known distribution, it means the observation model and the known model may share similar distribution. For some distributions (e.g., normal, uniform, logistic, exponential) there is only one possible value for the skewness and the kurtosis, and they are represented by a single point on the plot. For

other distributions, areas of possible values are represented in larger areas. It must be noted that the skewness and kurtosis, like all higher moments, have a very high variance and are not unique. Thus, a nonparametric bootstrap procedure was performed to consider the uncertainty of the estimated values of kurtosis and skewness from data [54]. Values of skewness and kurtosis are computed on bootstrap samples (constructed by random sampling with replacement from the original data set) and reported on the skewness-kurtosis plot. In this study, 500 bootstrap samples were defined.

We employed two goodness of fit plots, namely density plot and probability-probability (P–P) plot, to evaluate the ability of different nominated distribution functions in capturing the variability of data for each class of degree of saturation. A density plot represents the density function of the fitted distribution along with the histogram of the empirical distribution and can be regarded as a more basic and classical approach in evaluating the goodness of a fitted distribution. A P–P plot is a probability plot representing the empirical distribution function evaluated at each data point (y-axis) against the fitted distribution function (x-axis). It is used for assessing how closely two data sets agree, representing the empirical distribution function evaluated at each data point (y-axis) against the fitted distribution function (x-axis). The P–P plot emphasizes the lack-of-fit at the distribution center [55]. The comparison line is a straight line starting from (0,0) ending at (1,1). The empirical and theoretical distributions are equal if and only if the plot is located on this line; any deviation indicates a difference between the distributions.

### 5.1. Statistical analysis of measured wave velocities

#### 5.1.1. Shear wave velocity

Figs. 6a and 7a represent the CFG and histogram of holistic $v_s$ dataset, respectively, over the experimental range of saturations (i.e., the degree of saturation is constrained physically to nominally between 0 and 80%). Table S1 (Supporting Information) provides the summary statistics of the measured $v_s$ data, Fig. 4a. For the considered degrees of saturation, $v_s$ has the mean value of 116.30 (m/s) and standard deviation of 11.43 (m/s), which imply the coefficient of variation of almost 10% wherein no considerable variation is recognized in the holistic dataset. Fig. 7a illustrates that the distribution is more concentrated on the left of the figure and the right tail is longer and the positive skewness (0.38) implies that the mean and median of the data are greater than the mode, while the mode occurs at the highest frequency of which is located on the left side of the figure and for lower values of $v_s$. As the holistic dataset has a Kurtosis of 1.94, a uniform distribution could readily be assumed (Fig. 6a), in which a mean $v_s$ of 116.3 m/s would then be used in subsequent analyses; thereby neglecting any $v_s$-saturation relationships. However, it is evident from the experimental data that a $v_s$-saturation relationship exists (Fig. 4a), and the distribution about any saturation binned section of the data may not share the same Kurtosis and skewness or appearance of a uniform distribution. Thus, to quantify the functional form of the $v_s$-saturation relationship, the statistical distribution of the $v_s$ data as a function of degree of saturation, $S$, must be well defined. Therefore, the data have been binned into 4 different categories according to the corresponding nominal $S$ values: 0–20, 20–40, 40–60, and 60–80%. The decision of a uniform bin size of 20% saturation to statistically analyze the measured data was determined through consideration of the governing mechanisms and underlying theories of wave propagation in unsaturated soils in conjunction with where slope changes within the measured velocity (Fig. 4), SWRC (Fig. 1) and elastic moduli data (Fig. 5) are observed. For example, in Fig. 5A the $v_p/v_s$ ratio remains relatively constant until $S \approx 20\%$ and then retains a relatively constant rate of increase until the inflection point of the S-curve ($S \approx 40\%$), decreases from the inflection point to a highly saturated soil ($S \approx 60\%$) corresponding to observed viscoelastic behavior [16] wherein no further change in the $v_p/v_s$ ratio is observed through the maximum saturation ($S \approx 80\%$). Similar observations are made for different data. Therefore, the choice of four bins was best representative of the data and could be divided into regions corresponding with fundamental changes within the soil structure. The first region is at the residual suction state (corresponding to S = 0–20%) where the pendular state is discontinuous. The second is the region is that of higher suction (5–9 kPa) wherein water continuity is initially observed throughout the specimen (S = 20–40%) and suction has the most influence within the funicular state. The third region is that of low suction (3–5 kPa) wherein suction has less influence within the funicular state (S = 40–60%) and the fourth region is that of the nearly saturated soil (S = 60–80%) with negligible suction (less than 3 kPa) wherein the air phase is in the form of entrained air bubbles and is not continuous throughout the specimen. Recent research in shallow near-surface soils (less than 1 m in depth) shows that full saturation (S > 85%) is not achievable for these sands without the influence of significant confinement (in excess of 25 kPa) and backpressure saturation techniques [16, 33,56].

A parametric sweep of distribution types was performed to fit an appropriate distribution to the data for each category (Fig. 8). The goodness of fit was tested comparing the density plot (Fig. 8) and P–P plot (Fig. S1, Supporting Information). As seen, lognormal distribution can best fit the data over different ranges of saturations and the normal distribution (that would have been assumed from the holistic data) yields the lowest goodness of fit. The highest value of $v_s$ is 141 m/s when

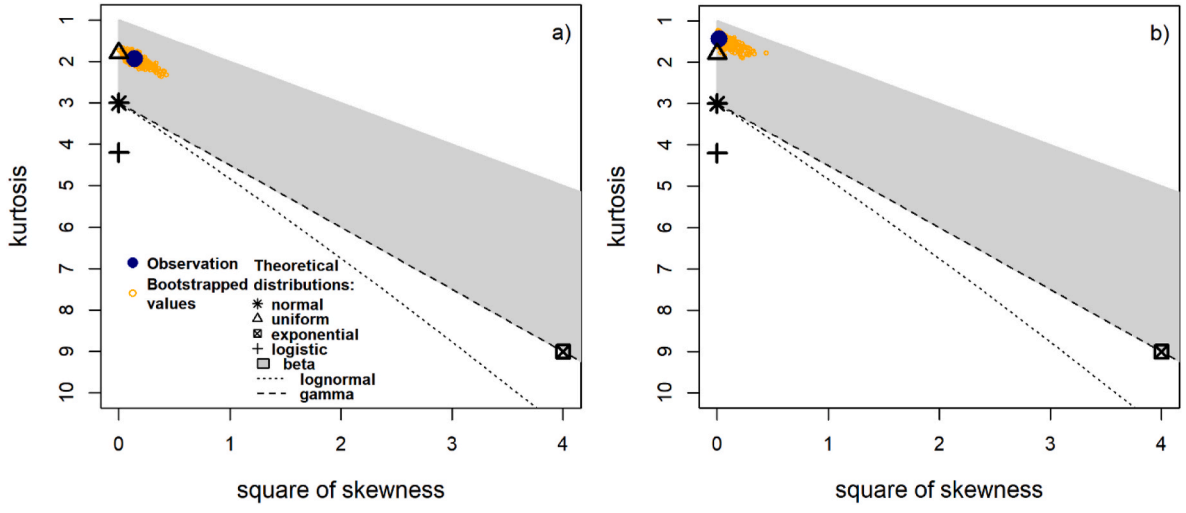


**Fig. 6.** Cullen and Frey graphs for the entire measured $v_s$ data (**a**) and $v_p$ data (**b**) across different degrees of saturation.

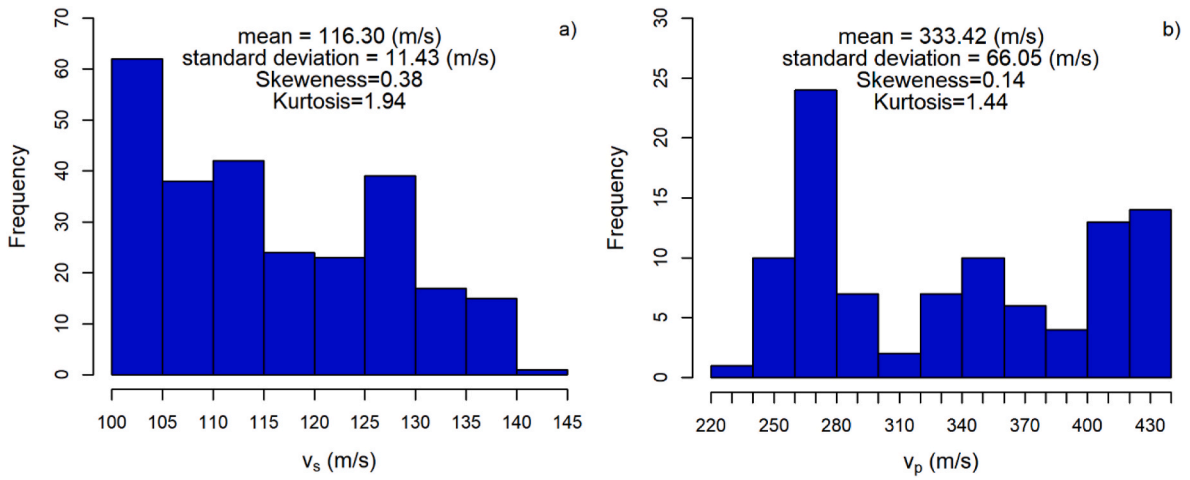


**Fig. 7.** Histogram plots for the entire measured $v_s$ data (**a**) and $v_p$ data (**b**) across different degrees of saturation.

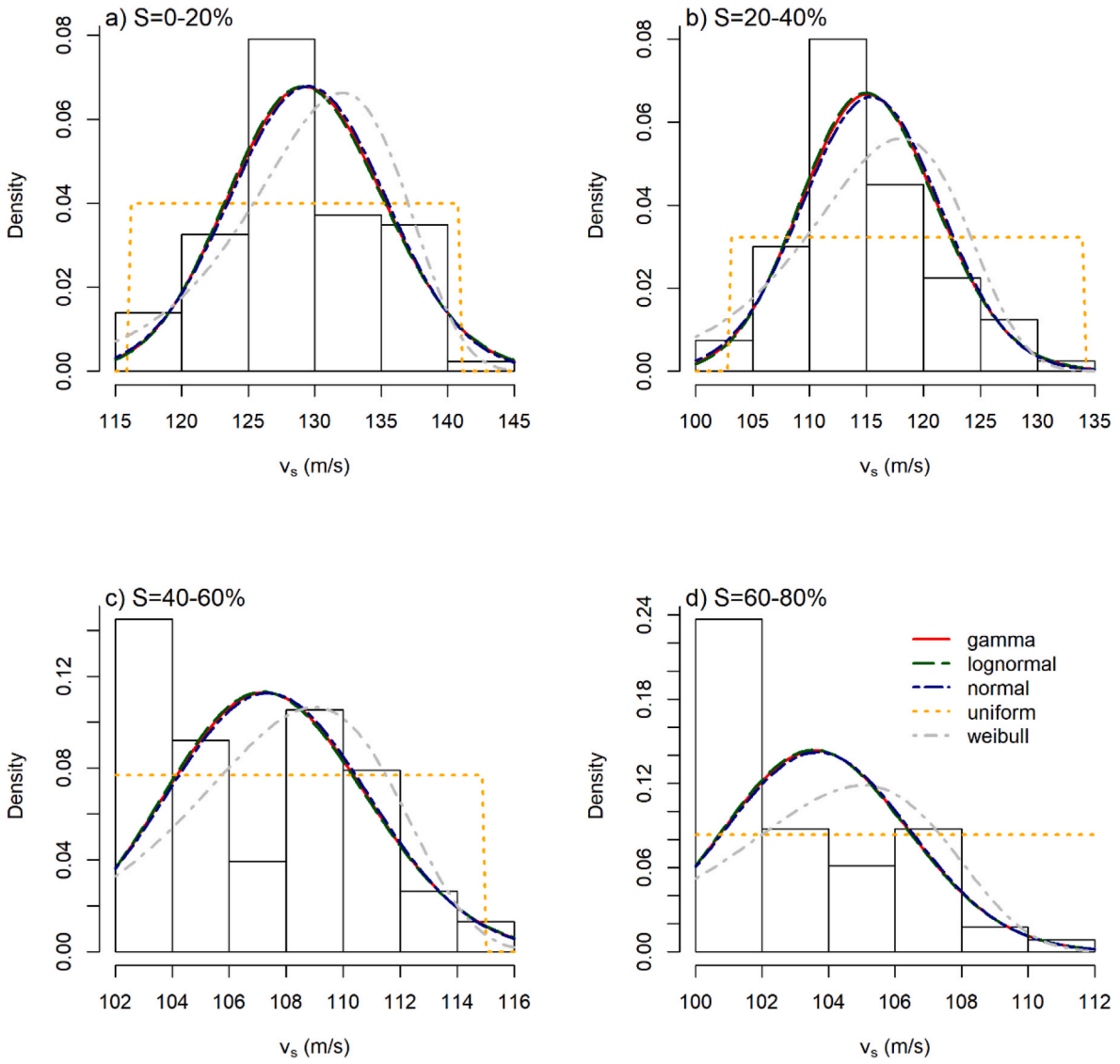


**Fig. 8.** Goodness-of-fit plots for various distributions fitted to measured $v_s$ data for different degrees of saturation intervals based on the density plots.

it is between 0 and 20% saturated, and its minimum value is 100 m/s when soil has a degree of saturation between 60 and 80%. It is noted the variation in values of $v_s$ dramatically decreases as the soil achieves a higher degree of saturation, and in such state shear waves attain a unique velocity in the soil.

### 5.1.2. Compressional wave velocity

The CFG and histogram of measured $v_p$ data are shown in Figs. 6b and 7b, respectively. Table S2 (Supporting Information) presents summary statistics of measured $v_p$ data. As seen, the data are widely distributed over the range between 220 and 440 m/s due to the high functional dependency on saturation than suction. The data have the mean of 333.42 m/s, standard deviation of 66.05 m/s, and a coefficient of variation of 20%. The skewness of 0.14 suggests that the holistic $v_p$ data are more symmetrically distributed compared to the $v_s$ data. The kurtosis of the holistic data (1.44) is considerably lower than 3.0 and suggests that the holistic data might be best represented by a uniform distribution. As with the $v_s$ data, a holistic distribution would ignore any $v_p$-$S$ relationships, clearly evidenced by Fig. 4b.

The holistic data were binned into the same 4 bins as the $v_s$ data. As shown in Fig. 9 and Fig. S2 (Supporting Information), in general, a Weibull distribution can best capture the variability of data for different $S$. Fig. 9 and Table S2 suggest that there is a considerable $v_p$ variability over different $S$ magnitudes. It is in contrast with the literature, which states not much variation in the compressional wave velocity occurs unless around the air entry pressure. It is noted for the soil tested in this study, the air entry pressure corresponds to degree of saturation above 90%.

Table S2 demonstrates that the standard deviation of the data first increases with increase in the degree of saturation and then decreases as soil moves toward saturation. More specifically variability of the data is the lowest for those obtained in degrees of saturations above 60% and below 20% suggesting that unique values of $v_p$ exist at the boundaries of the $v_p$-saturation relationships. Research by Taylor et al. [16] observed that for unconfined specimens, of the same sand, at saturation degrees above 70% the internal soil structure started to behave like a non-Newtonian fluid and led to the collapse of the specimen (e.g., see Ref. [16]). This observation was confirmed for both static and dynamic pore fluid at low confinement in Ref. [57]. Therefore, it was expected for $v_p$ to try and achieve, with an increase in saturation, a relatively constant value with minimal variability as confirmed in Fig. 4b.

As for the dry state (0–20% saturation) we would expect an equally low standard deviation as the pore space is mainly occupied by air rather than water, as confirmed in Fig. 4b. This, and the fact that the tests were

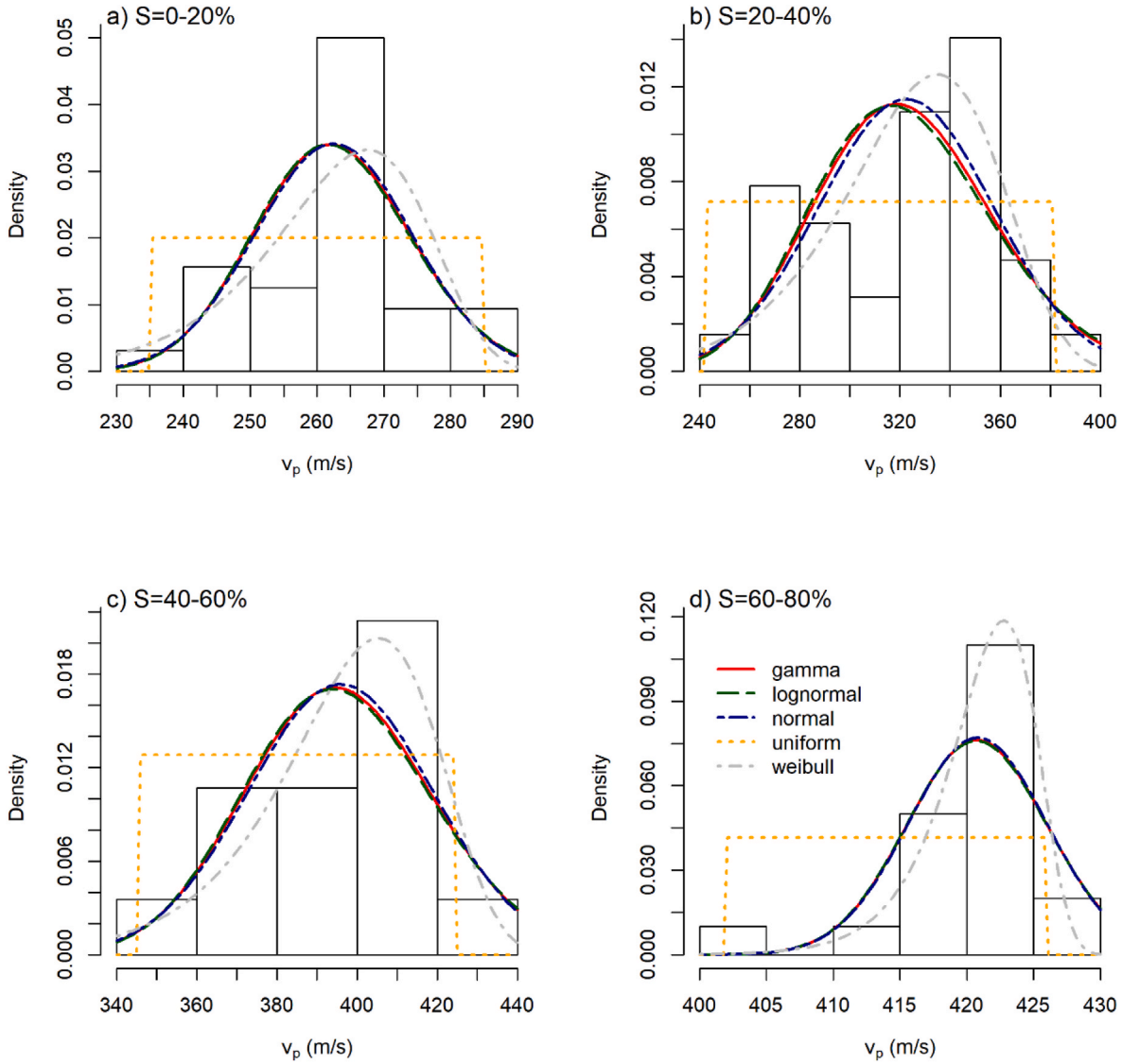


**Fig. 9.** Goodness-of-fit plots for various distributions fitted to measured $v_p$ data for different degrees of saturation intervals based on the density plots.

performed under zero confining pressure, explains why the measured velocities are considerably lower than $v_p$ in air (330 m/s) and is supported within the literature (e.g., Ref. [58]). This trend is more pronounced for the data below 13% saturation, where the rate of changes of matric suction with degree of saturation is minimum (the residual saturation points). The reason that the standard deviation is larger than what we see at the high saturation range is because the 0–20% saturation bin includes the initial point where the pore fluid starts to impact the soil matrix, or in other words, the volumetric water content exceeds the residual water content and the effects of the SWRC on the soil

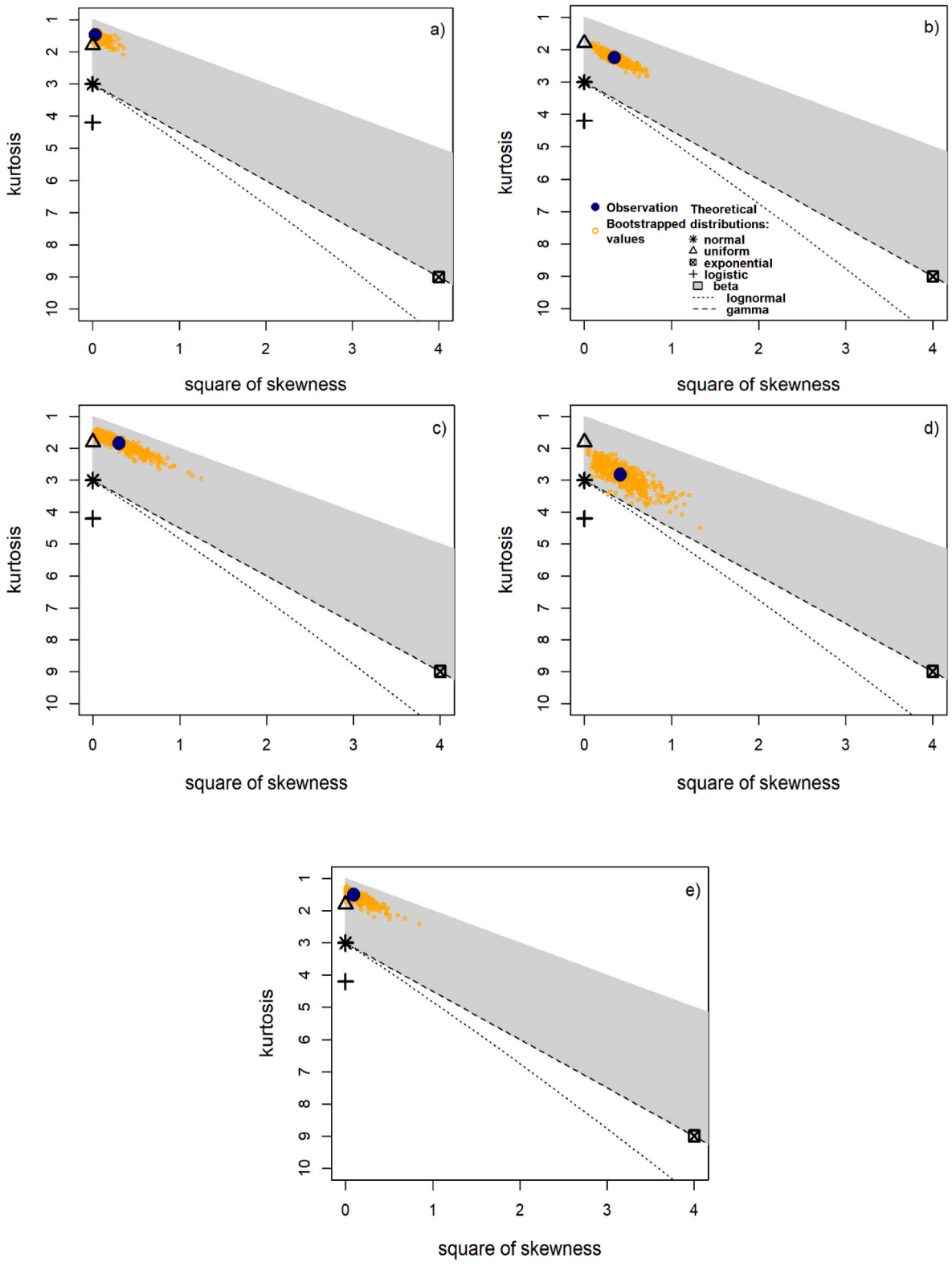


**Fig. 10.** Cullen and Fey Graphs for (**a**) $v_p/v_s$ ratio for the correlated $v_p$ and $v_s$ measurements; (**b**) derived values of G versus $S$, from Eq. (1); (**c**) derived values of $\mu$ versus $S$ from Eq. (2); (**d**) derived values of E versus $S$ from Eq. (3); (**e**) derived K versus $S$ from Eq. (4).

structure are first encountered.

### 5.2. Derivation and statistical analysis of elastic moduli

#### 5.2.1. The $v_p/v_s$ ratio

Fig. 5a depicts the $v_p/v_s$ ratio for the 98 correlated $v_p$ and $v_s$ measurements from Fig. 4. Observed in Fig. 5a, the soil takes on a predominately saturated state ($v_p/v_s > 3.5$) when the saturation exceeds 50%. For this material the minimum $v_p/v_s$ ratio measured is 1.81 but is reasonable based on the typical assumptions for near-surface seismic surveys (i.e., $v_p/v_s \approx 2.0$) and for the observed stiffness during self-supported unconfined drained testing of dry sands (e.g., Ref. [57]).

Figs. 10a and 11a show the CFG and histogram of the derived $v_p/v_s$ values, respectively. The holistic data has the mean value of 2.94, corresponding to $\mu$ of 0.43, and standard deviation of 0.82. The data exhibit the considerable coefficient of variation of 28%. Although, it is shown that $v_p/v_s$ for each soil varies with $S$ (e.g., Refs. [16,59]), such variations were within a narrow range. While, the current study shows that this

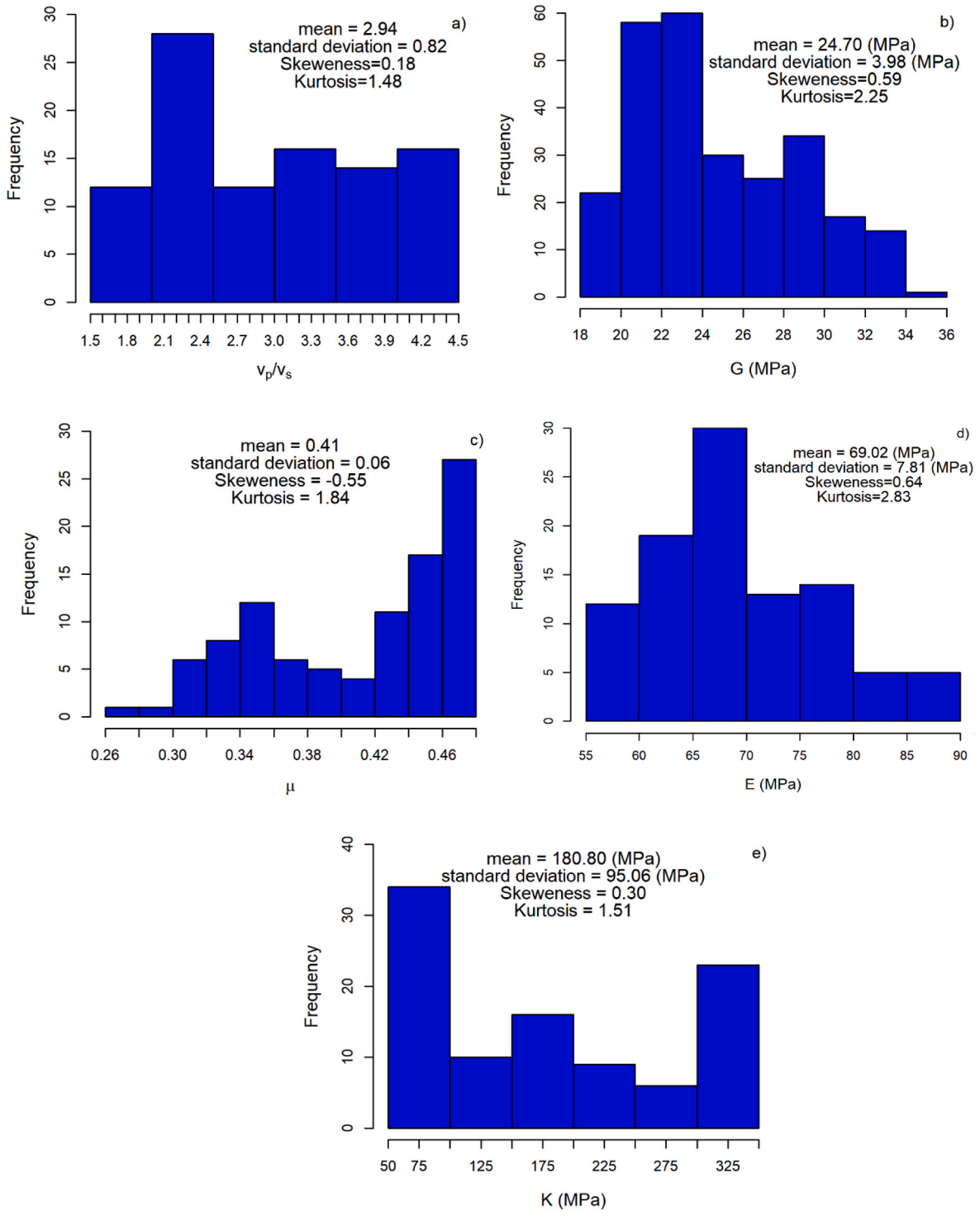


**Fig. 11.** Histograms for (**A**) $v_p/v_s$ ratio for the correlated $v_p$ and $v_s$ measurements; (**B**) derived values of G versus $S$, from Eq. (1); (**C**) derived values of $\mu$ versus $S$ from Eq. (2); (**D**) derived values of E versus $S$ from Eq. (3); (**E**) derived K versus $S$ from Eq. (4).

ratio can vary from low value of 1.5 to considerably higher values up to 4.3. Fig. 11a demonstrates that the distribution of the holistic data cannot be captured with any of the well-known distributions. Thus, the data has been divided into the same 4 saturation bins. Fig. 12 and Fig. S3 (Supporting Information) suggest that both normal and logistic distribution can be good candidates to fit the data with. As shown in Fig. 12 and Table S3, $v_p/v_s$ has a direct relation with $S$ and increases as the soil moves toward saturation. This trend can be explained by variation in $v_p$ and $v_s$. It was stated previously that variation of $v_s$ with degree of saturation was not considerable since this dynamic property is more affected by suction stress, and the tested soil could not develop high suction values over a major range of saturations. While, the measured $v_p$ exhibited up to 60% variation between different degrees of saturation. Results also specify that variation of the data is minimum when the soil has degree of saturation between 0 and 20 or 60–80%, which can be explained by the relative uniqueness of $v_p$ and $v_s$ in these regions. It must be highlighted that $v_p/v_s$ does not share the same type of distribution with $v_p$ or $v_s$, though $v_p$ seems to be dominant and govern the ratio of the wave velocities.

### 5.2.2. Shear modulus

Fig. 5b depicts the shear modulus, $G$, determined using the shear wave velocity measurements along with Eq. (1) versus $S$ (total of 252 data points are shown in the figure). It is observed that $G$ decreases as $S$ increases, eventually reaching a plateau when $S > 80\%$. As expected, the trend is identical to that seen in the measured $v_s$ data.

The holistic statistical variation of $G$ for different $S$ are presented in Figs. 10b and 11b. Higher frequency of the data is located on the left side of the histogram (Fig. 11b). It is because of the direct relation between $v_s$ and $G$, and the fact that the measured $v_s$ does not experience significant variation until the soil approaches the residual (dry) state. Holistically, the data has a coefficient of variation of 16%; significantly higher than that of $v_s$. Fig. 10b indicates that the variation of the holistic data cannot be captured with any theoretical distributions, therefore the data is binned identically to the base $v_s$ measurements.

Figs. 13 and S4 (Supporting Information) demonstrate that the variation in the data for different saturation bins can be reasonably predicted with a lognormal fit; the same type of distribution as the $v_s$ which is expected considering their relationships, Eq. (1), summarized in Table S4 (Supporting Information). As $G$ is a measure of soil stiffness, directly related to the matric suction and effective stress, and is proportional to the square of $v_s$, $G$ is expected to reach its lowest when the soil is fully saturated and the highest when the soil is in the dry state. Highest variation in the data is expected to be observed around the air

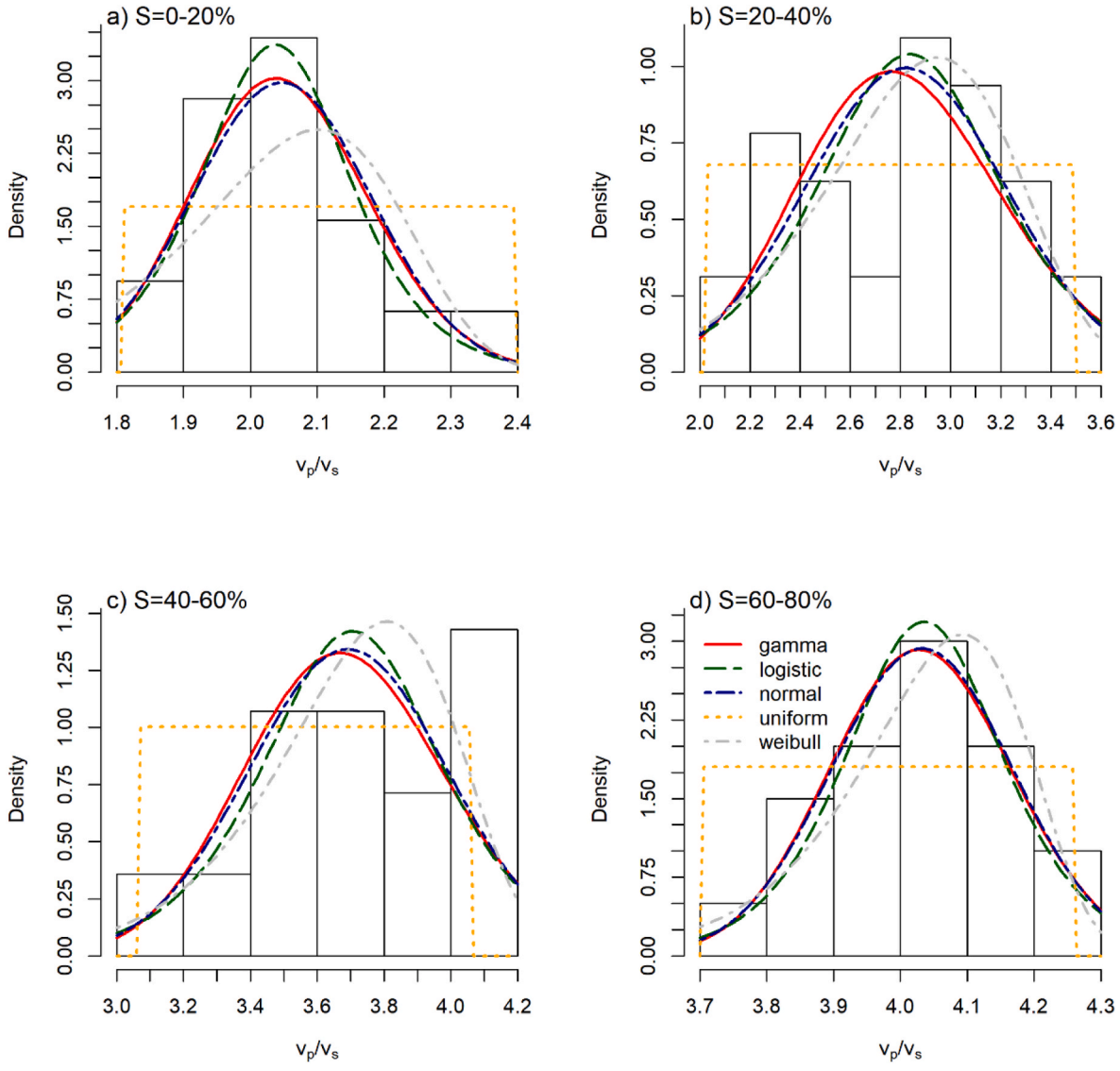


**Fig. 12.** Goodness-of-fit plots for various distributions fitted to $v_p/v_s$ data for different degrees of saturation intervals based on the density plots.

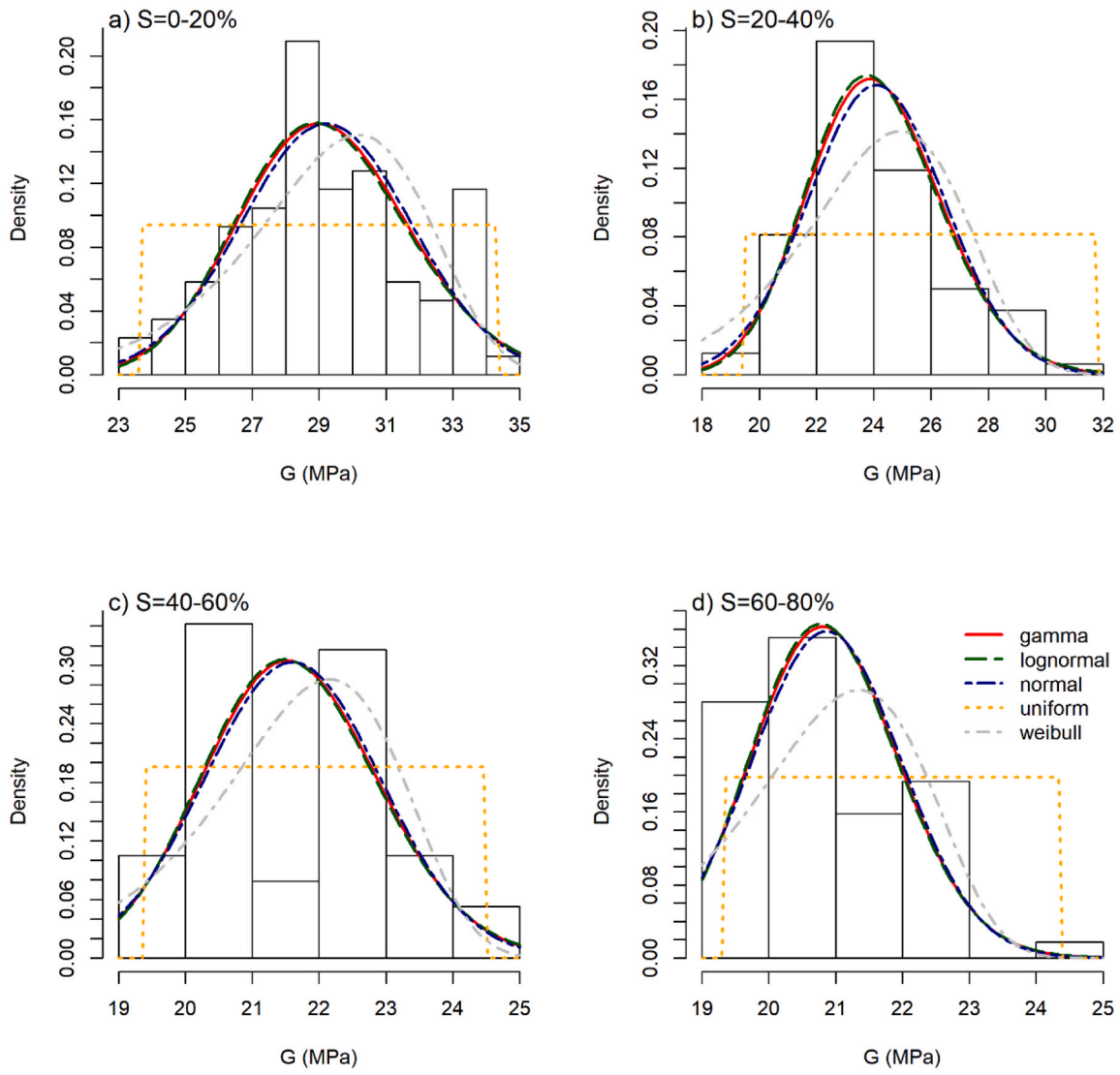


**Fig. 13.** Goodness-of-fit plots for various distributions fitted to derived shear modulus data for different degrees of saturation intervals based on the density plots.

entry value, i.e., when the soil starts to desaturate (drying). Based on the SWRC, Fig. 1, this should occur at a degree of saturation above 90%, which is not achievable without the application of external confining pressures not experienced in-situ. For this study, the effective fully saturated condition occurs at $S \approx 70\%$, after which the variation of $G$ with degree of saturation becomes less significant. As the soil continues to move toward the dryer states (0–60%), suction stress (Fig. 1) increases corresponding to an increase in the rate of change in $G$ and is consistent with the existing literature [31].

### 5.2.3. Poisson's ratio

Fig. 5c clearly illustrates that there is a significant $\mu$-$S$ relationship, i.e., the assumption of constant $\mu$ is not valid. A similar observation was made by Thota et al. [18], who proposed the concept of Poisson's ratio characteristic curve (PRCC) by employing a sigmoidal function to establish a $\mu$-$S$ relationship between $\mu$ and $S$ (or $\mu$ and $\psi$). However, as $S$ increases (in excess of 40%) there is negligible change in both the magnitude and uncertainty of $\mu$ with increased $S$, i.e., the $\mu$-$S$ relationship becomes relatively constant with negligible deviation within the derived dataset.

The best fit distributions (Fig. 10c) and histogram (Fig. 11c) for the holistic derived $\mu$ dataset yield a mean of 0.41 and a standard deviation of 0.06, resulting in a coefficient of variation of 15%; which is in between those of $v_s$ (10%) and $v_p$ (20%). The holistic data displays a negative skewness of −0.55 that implies that the mode is greater in magnitude than (and located to the right of) the mean and median. This observation can be explained by the relationship between $\psi$ and $\mu$, wherein both $\psi$-water content curve and $\mu$ -water content curve have sigmoidal shapes and $\mu$ is maximum where $\psi$ is minimum and vice versa [18]. Similar to $\psi$, $\mu$ varies between dry and saturated states wherein, $\mu$ is minimum in lower $S$ due to high compressibility of dry soil and is maximum when the soil is saturated. It is shown experimentally that when soil starts to desaturate, $\mu$ decreases with different rates depending on the dominant water retention state [26,59–61].

In this study, the tested soil consists of large particles with low plasticity, thus capillary is the main mechanism of water retention in soil and changes in $\mu$ should be minimal. It is expected for the $\mu$ to sharply increase as the volumetric water content becomes greater than the residual value (~13% saturation) and reach a plateau for higher volumetric water contents (degrees of saturation). Fig. 10c demonstrates that none of the theoretical distributions can capture the variability of the holistic data set. Therefore, the data is again binned into 4 saturation ranges based on the SWRC; Figs. 14 and S5 (Supporting Information) show the best fit (Weibull) to the binned data, the same distribution type as the $v_p$. Such observations can be explained by the dependency of $\mu$ with $v_p^{\,2}/v_s^{\,2}$ and low variability of $v_s$ compared to $v_p$. However, it must

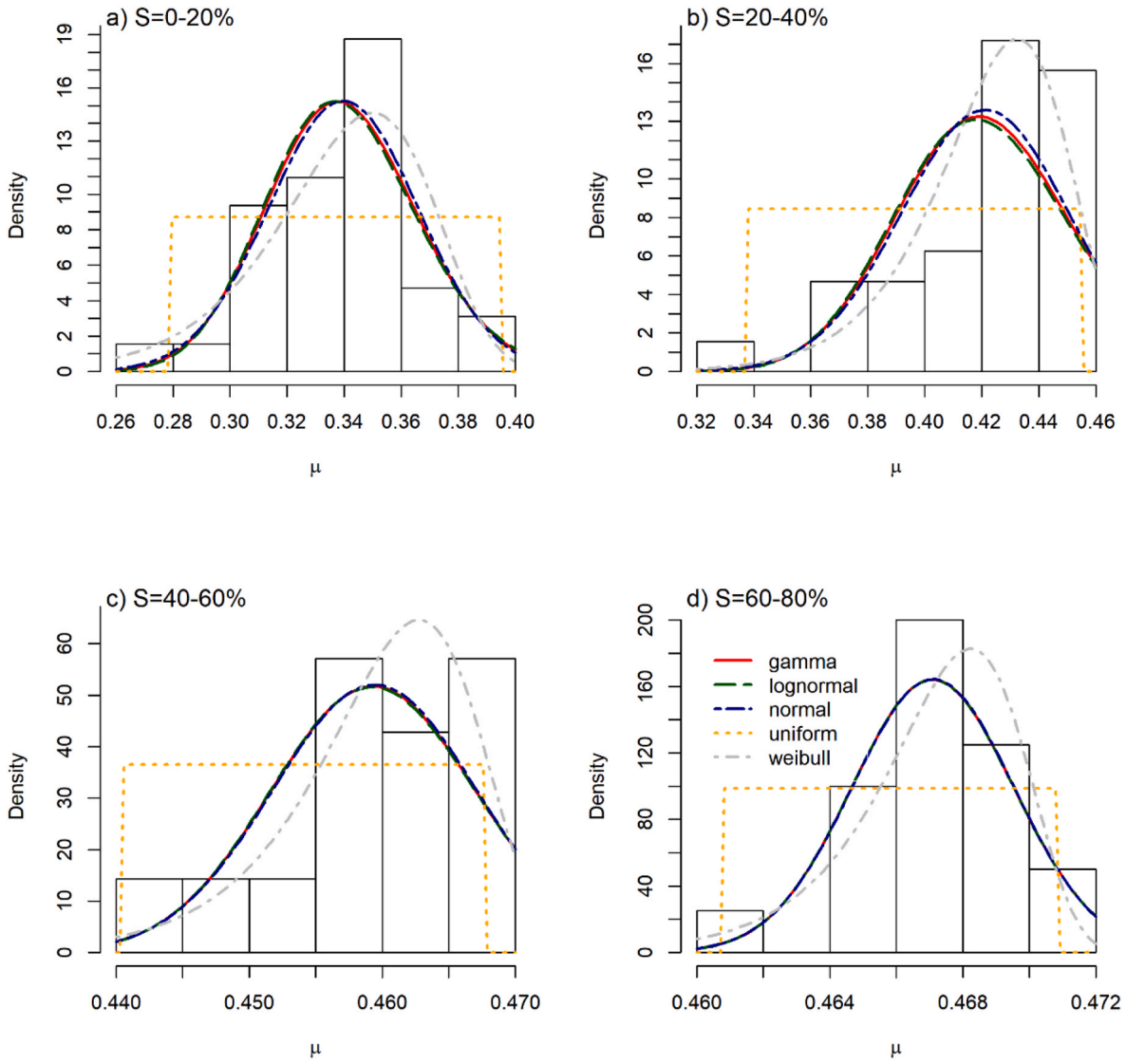


**Fig. 14.** Goodness-of-fit plots for various distributions fitted to derived $\mu$ data (Eq. (2)) for different $S$ intervals based on the density plots.

be noted that parameters of the Weibull distribution significantly differ for the derived $\mu$ and $v_p$. Furthermore, the $\mu$ data are highly skewed to the left compared to $v_p$ and $v_s$, Table S5 (Supporting Information), wherein the standard deviation of the data is highest at low degree of saturations and drops significantly, becoming almost zero approaching higher degrees of saturation when capillary is the dominant mechanism of water retention.

### 5.2.4. *Young's modulus*

Fig. 5d illustrates the *E-S* relationship for the derived data (Eq. (3)), wherein a decreasing trend is observed. The holistic data, Fig. 5d, has the mean value of 69.02 MPa, standard deviation of 7.81, coefficient of variation of 11.5%, and is positively skewed, which is reasonable due to the soil type and its inability to develop high suction unless for moisture content below the residual water content. Fig. 10d shows the best fit options for the derived holistic $E$ data wherein the skewness and kurtosis of the data varies significantly from the theoretical distributions with no singular distribution type being representative of the holistic dataset; e.g., the distribution can be simulated using either normal, gamma, or lognormal distributions. Binning the data, Figs. 15 and S6 (Supporting Information), demonstrates that the predominant kurtosis is approximately 3.0 (Table S6), which corresponds to a normal distribution that yields the same level of data outliers and might be a good candidate to fit the data. However, it should be noted that for the lower suction values (40–60% saturation) a Weibull distribution is a better fit of the derived data.

### 5.2.5. *Bulk modulus*

The magnitude of $K$, Eq. (4), can be used to define the change in shape of a soil element at constant volume and is functionally dependent on $G$ and the square of the $v_p/v_s$. In elasticity, $K$ defines the volumetric component of elastic deformation and, similarly to $G$, is vital in understanding wave propagation and attenuation, reconstruction of energetic source properties, signal processing, and soil-sensor interactions and coupling effects. The magnitude of $K$ is lowest when the pore space is filled with air (compressible media) and largest when saturated (incompressible media) with unique values of $K$ at saturations less than the residual saturation (0–20%) and at the effective saturated condition (60–80%); derived $K$ data is presented in Fig. 5e.

Figs. 10e and 11e show the best fit candidates and histogram of the holistic derived $K$ dataset, Fig. 5e, respectively. Considering the relation between the $K$ and the $v_s$ and $v_p$ measurements it is expected to observe similar distribution characteristics, however, Fig. 11e shows that the distribution of the holistic derived $K$ dataset differs considerably from the holistic $v_s$ and $v_p$ distributions. The holistic data has a mean of 180.80 MPa and standard deviation of 95.06 MPa. These two values

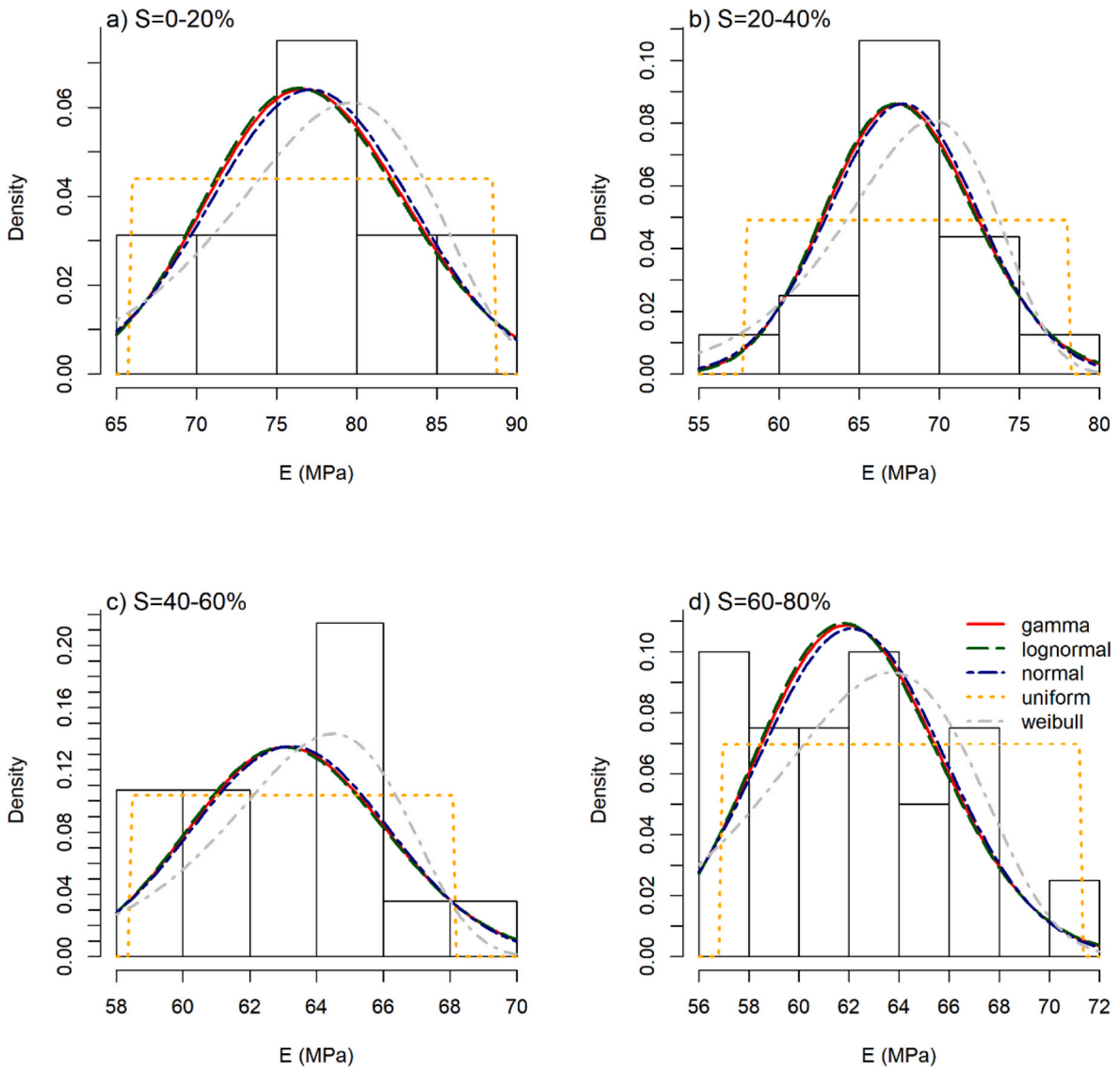


**Fig. 15.** Goodness-of-fit plots for various distributions fitted to derived Young's modulus, $E$, data for different degrees of saturation intervals based on the density plots.

indicate the coefficient of variation of 50%, which is about 5 and 2.5 times greater than coefficient of variation of $v_s$ and $v_p$ respectively. The holistic $K$ dataset, though, expresses a skewness of 0.30 (close to zero) but is not normally distributed, but rather symmetrical with highest frequency in both tails, Fig. 10e, suggesting that the resulting distributions do not share the same skewness and kurtosis with any theoretical distribution; i.e., no single distribution can be fitted to the data distribution and requires the data to be binned. Figs. 16 and S7 (Supporting Information) shows a comparison between different distributions fitted to the data for different saturation ranges, wherein the post residual saturations ($S > 20\%$) can best be fit with a Weibull distribution. In the residual state, the data variability is best represented by a lognormal distribution. This observation is in keeping with the distributions within the controlling states: in the residual regime the pore fluid does not achieve continuity throughout the soil thus the ability to resist volumetric change is governed by the soil structure ($v_s$), conversely when the pore fluid is continuous throughout the soil the incompressibility of the fluid will increasingly resist volume change thereby governed by $v_p$. Even though the $v_p$ and $K$ share the same distribution type, the distribution characteristics, i.e., shape factor and scale factor for Weibull distribution, are significantly different, Table S7, and the mean and median are close for different saturation ranges which shows that the data are symmetrically distributed around the mean.

## 6. Conclusions

In this study, we investigated the statistical variance of $v_p$- and $v_s$-saturation relationships and their derived moduli based 360 laboratory tests performed on a washed, poorly graded, fine-to-medium quartz-silica beach sand over seven full wetting-drying cycles (representing repetitive natural meteorological events). Consistently for all measured and derived properties, the statistical interpretations of the holistic data do not adequately represent the saturation relationships and must be appropriately binned for any statistical analyses. The requirement to bin the data to appropriately account for the saturation relationships negates the assumption that $v_p$- and $v_s$ measurements and elastic moduli can be assumed constant or that an arithmetic mean is best representative value of the desired parameter.

The statistical analyses showed that the $v_p$ and $v_s$ data (binned) are best represented by lognormal and Weibull distributions, respectively, with a uniqueness (i.e., minor standard deviation) in residual and saturated magnitudes at both saturation tails. The results of the $v_p/v_s$

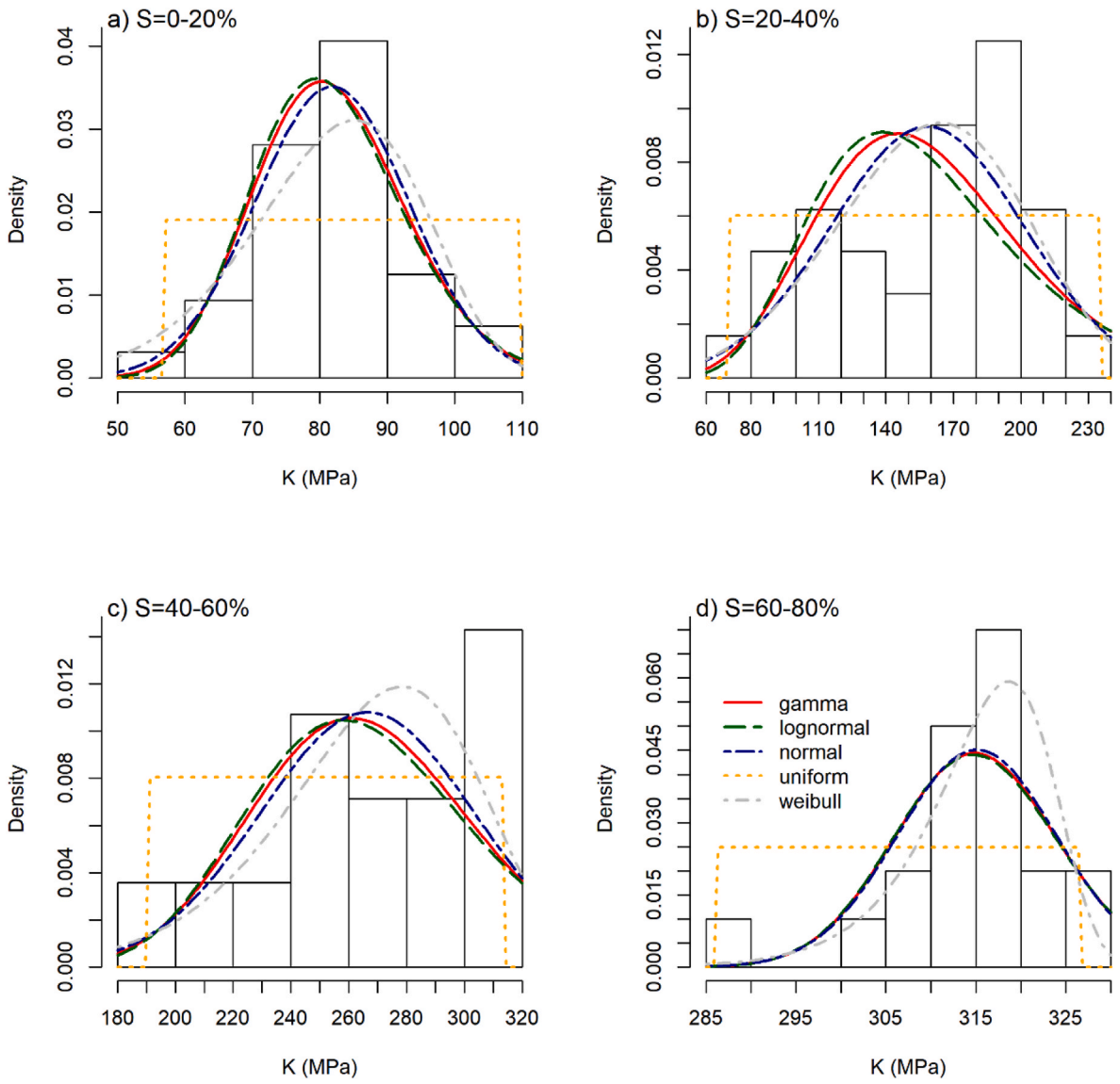


**Fig. 16.** Goodness-of-fit plots for various distributions fitted to bulk modulus data for different degrees of saturation intervals based on the density plots.

ratio indicate that a similar uniqueness to that of the $v_p$ and $v_s$ saturation tails, however, the binned $v_p/v_s$ data is best represented by a normal or lognormal distribution. The statistical distribution of $G$ (lognormal) is similar to that of the governing $v_s$ data. In the elastic derivation of $G$, the uniqueness within the residual regime is lost and the highest variability is observed which is inconsistent with the observations of the governing binned $v_p$ and $v_s$ data. The saturated regime retains similar uniqueness as the governing $v_s$ data. Young's modulus is predominantly represented by a normal distribution, except in the lower suction regime (40–60% saturation) wherein the Weibull distribution provides a better fit (suggesting that the $v_p$ is the dominate factor governing the statistical and physical behavior within the soil). Similarly, for $\mu$, the statistical variability is highest for the residual regime but becomes negligible for saturation above 50% wherein the experimental data converges to a discrete $\mu$-saturation curve. However, the Weibull distribution governs the $\mu$ variability suggesting the physical governance of $v_p$. The distributions of K illustrate that the residual regime is governed by the $v_s$ both in terms of statistical variability (lognormal distribution) and physical behavior (i.e., with the lack of continuity of any incompressible pore fluid any resistance to volumetric distortion must come from granular friction and contact forces). In the other regimes, where pore fluid is continuous, the statistical distribution changes to a Weibull distribution and is governed predominately by the $v_p$.

The results indicate that many of the assumptions regarding the quantification of $v_p$- and $v_s$ measurements and elastic moduli used in geophysical, geotechnical, and geo-environmental analyses may not be valid; readily accounting for unexpected deviations between model and in-situ behavior despite ever increasing model complexities. While this work acknowledges the need to investigate more soils, in light of these findings, the material specifically chosen for this study was to minimize the influence of $\psi$ such that if significant statistical variabilities are observed (as is the case) thereby it can be readily assumed that the amplitude of the variability will only increase with larger magnitudes of. $\psi$.

## Author statement

**Oliver-Denzil S. Taylor:** Conceptualization, Methodology, Validation, Formal analysis, Investigation, Writing – Original Draft, Writing – Review & Editing, Visualization, Funding acquisition.

**Masood Abdollahi:** Formal analysis, Investigation, Writing – Original Draft, Writing – Review & Editing, Visualization.

**Farshid Vahedifard:** Conceptualization, Methodology, Formal analysis, Writing – Original Draft, Writing – Review & Editing,

Visualization, Funding acquisition.

## Data availability statement

All data and information relevant to this article will be made available before publication.

## Declaration of competing interest

The authors declare that they have no known competing financial interests or personal relationships that could have appeared to influence the work reported in this paper.

## Acknowledgment

The authors would like to acknowledge W.W. Berry, A.L. Cunningham and L.A. Walshire for the assistance in executing the physical experiments. This material is based upon work supported in part by the National Science Foundation (NSF) under Grant No. CMMI-1634748 and Assistant Secretary of the Army (Acquisition, Logistics, and Technology (ASA(ALT)) under the Future Innovations Funds Directed Research (FLEX-4) Program "Unlocking the Physics of Near-Surface Soil Mechanics". Permission to publish was granted by Director, Geotechnical and Structures Laboratory, U.S. Army Engineer Research and Development Center, with unlimited distribution.

## Appendix A. Supplementary data

Supplementary data to this article can be found online at https://doi.org/10.1016/j.soildyn.2022.107247.

## References

[1] Adamo F, Attivissimo F, Fabbiano L, Giaquinto N, Spadavecchia M. Soil moisture assessment by means of compressional and shear wave velocities: theoretical analysis and experimental setup. Measurement 2010;43:344–52. https://doi.org/10.1016/J.MEASUREMENT.2009.11.007.

[2] Koper KD, Wallace TC, Aster RC. Seismic recordings of the carlsbad, New Mexico, pipeline explosion of 19 august 2000. Bull Seismol Soc Am 2003;93:1427–32.

[3] Catchings RD, Rymer MJ, Goldman MR, Sickler RR, Criley CJ. A method and example of seismically imaging near-surface fault zones in geologically complex areas using VP, VS, and their ratios. Bull Seismol Soc Am 2014;104:1989–2006. https://doi.org/10.1785/0120130294.

[4] Aleardi M. The importance of the Vp/Vs ratio in determining the error propagation, the stability and the resolution of linear AVA inversion: a theoretical demonstration. Boll Di Geofis Teor Ed Appl 2015;56:357–66.

[5] Alam MI, Jaiswal P. Near surface characterization using VP/VS and Poisson's ratio from seismic refractions. J Environ Eng Geophys 2017;22:101–9. https://doi.org/10.2113/JEEG22.2.101.

[6] Essien UE, Akankpo AO, Igboekwe MU. Poisson's ratio of surface soils and shallow sediments determined from seismic compressional and shear wave velocities. Int J Geosci 2014;5:1540.

[7] Fortin J, Guéguen Y, Schubnel A. Effects of pore collapse and grain crushing on ultrasonic velocities and Vp/Vs. J Geophys Res Solid Earth 2007;112. https://doi.org/10.1029/2005JB004005.

[8] Zimmer M, Prasad M, Mavko G. Pressure and porosity influences on VP−VS ratio in unconsolidated sands. Lead Edge 2002;21:178–83. https://doi.org/10.1190/1.1452609.

[9] Carr BJ, Hajnal Z, Prugger A. Shear-wave studies in glacial till. Geophysics 1998;63:1273–84. https://doi.org/10.1190/1.1444429.

[10] Letson F, Barthelmie RJ, Hu W, Brown LD, Pryor SC. Wind gust quantification using seismic measurements. Nat Hazards 2019;99:355–77. https://doi.org/10.1007/s11069-019-03744-8.

[11] Inazaki T, Kaneko M, Aoike K. Detailed geophysical imaging OF the shallow surfaces at an UNDERSEEPAGE site behind OF a levee. Symp Appl Geophys Eng. Environ Probl 2016 Soc Explor Geophysicists Environ Eng Geophys Soc 2016:90–5. https://doi.org/10.4133/SAGEEP.29-020.

[12] Bonner J, Waxler R, Gitterman Y, Hofstetter R. Seismo-acoustic energy partitioning at near-source and local distances from the 2011 sayarim explosions in the negev desert, Israel. Bull Seismol Soc Am 2013;103:741–58. https://doi.org/10.1785/0120120181.

[13] Hassanizadeh SM, Celia MA, Dahle HK. Dynamic effect in the capillary pressure–saturation relationship and its impacts on unsaturated flow. Vadose Zone J 2002;1:38–57. https://doi.org/10.2113/1.1.38.

[14] Lu Z, Sabatier J. Effects of soil water potential and moisture content on sound speed. J Acoust Soc Am 2009;125:2520. https://doi.org/10.1121/1.4783475.

[15] Shen J, Crane JM, Lorenzo JM, White CD. Seismic velocity prediction in shallow (<30 m) partially saturated, unconsolidated sediments using effective medium theory. J Environ Eng Geophys 2016;21:67–78. https://doi.org/10.2113/JEEG21.2.67.

[16] Taylor O-DS, Cunningham AL, Martin KE, Walker Mhm& Pgk RE. Near-surface soils: ultrasonic near-surface inundation testing. Near Surf Geophys 2019;17:331–44.

[17] Vahedifard F, Thota SK, Cao TD, Samarakoon RA, McCartney JS. Temperature-dependent model for small-strain shear modulus of unsaturated soils. J Geotech Geoenviron Eng 2020;146:4020136. https://doi.org/10.1061/(ASCE)GT.1943-5606.0002406.

[18] Thota SK, Cao TD, Vahedifard F. Poisson's ratio characteristic curve of unsaturated soils. J Geotech Geoenviron Eng 2021;147:4020149. https://doi.org/10.1061/(ASCE)GT.1943-5606.0002424.

[19] Moss RES. Quantifying measurement uncertainty of thirty-meter shear-wave velocity. Bull Seismol Soc Am 2008;98:1399–411. https://doi.org/10.1785/0120070101.

[20] Biot MA. Theory of propagation of elastic waves in a fluid-saturated porous solid. I. Low-Frequency range. J Acoust Soc Am 1956;28:168–78. https://doi.org/10.1121/1.1908239.

[21] Biot MA. Theory of propagation of elastic waves in a fluid-saturated porous solid. II. Higher frequency range. J Acoust Soc Am 1956;28:179–91. https://doi.org/10.1121/1.1908241.

[22] Ishihara K, Huang Y, Tsuchiya H. Liquefaction resistance of nearly saturated sand correlated with longitudinal wave velocity. Poromechanics; 1998. p. 583–6.

[23] Valle-Molina C, Stokoe KH. Seismic measurements in sand specimens with varying degrees of saturation using piezoelectric transducers. Can Geotech J 2012;49:671–85. https://doi.org/10.1139/t2012-033.

[24] Le C, Cz Y. Effects of confining pressure and degree of saturation on wave velocities of soils. Int J GeoMech 2016;16:D4016013. https://doi.org/10.1061/(ASCE)GM.1943-5622.0000727.

[25] Flammer I, Blum A, Leiser A, Germann P. Acoustic assessment of flow patterns in unsaturated soil. J Appl Geophys 2001;46:115–28. https://doi.org/10.1016/S0926-9851(01)00032-5.

[26] Inci G, Yesiller N, Kagawa T. Experimental investigation of dynamic response of compacted clayey soils. Geotech Test J 2003;26:125–41. https://doi.org/10.1520/GTJ11328J.

[27] Alramahi B, Alshibli K, Fratta D, Trautwein S. A suction-control apparatus for the measurement of P and S-wave velocity in soils. Geotech Test J 2008;31:12–23. https://doi.org/10.1520/GTJ100646.

[28] Irfan M, Tu. Effects of soil moisture on shear and dilatational wave velocities measured in laboratory triaxial tests. In: 5th Int. Young Geotech. Eng. Conf. Adv. Soil Mech. Geotech. Eng.; 2013. p. 505–9. https://doi.org/10.3233/978-1-61499-297-4 -505. Amsterdam.

[29] Gao W, Watts CW, Ren T, Shin H-C, Taherzadeh S, Attenborough K, et al. Estimating penetrometer resistance and matric potential from the velocities of shear and compression waves. Soil Sci Soc Am J 2013;77:721–8. https://doi.org/10.2136/sssaj2012.0394.

[30] Tamura S, Tokimatsu K, Abe A, Sato M. Effects of air bubbles on B-value and P-wave velocity of a partly saturated sand. Soils Found 2002;42:121–9. https://doi.org/10.3208/sandf.42.121.

[31] Dong Y, Lu N. Dependencies of shear wave velocity and shear modulus of soil on saturation. J Eng Mech 2016;142:04016083. https://doi.org/10.1061/(ASCE)EM.1943-7889.0001147.

[32] Taylor OS, McKenna MH, Quinn MCL, Quinn BG. Partially saturated soil causing significant variability in near surface seismic signals. Near Surf Geophys 2014;12:467–80. https://doi.org/10.3997/1873-0604.2013039.

[33] Taylor O-DS, Walshire LA, Berry WW. Reducing uncertainties and improving sand soil-water retention curve (SWRC) predictions for hazard screening analyses. Can Geotech J 2020;57:1518–33. https://doi.org/10.1139/cgj-2019-0248.

[34] Zhang LL, Zhang LM, Tang WH. Rainfall-induced slope failure considering variability of soil properties. Géotechnique 2005;55:183–8. https://doi.org/10.1680/geot.2005.55.2.183.

[35] Li D-Q, Wang L, Cao Z-J, Qi X-H. Reliability analysis of unsaturated slope stability considering SWCC model selection and parameter uncertainties. Eng Geol 2019;260:105207. https://doi.org/10.1016/j.enggeo.2019.105207.

[36] Farshid V, JF H, TF T, Masood A, Aneseh A, Amir A. Levee fragility behavior under projected future flooding in a warming climate. J Geotech Geoenvironmental Eng 2020;146:4020139. https://doi.org/10.1061/(ASCE)GT.1943-5606.0002399.

[37] Abdollahi M, Vahedifard F. Model for lateral swelling pressure in unsaturated expansive soils. J Geotech Geoenviron Eng 2021;147:04021096. https://doi.org/10.1061/(ASCE)GT.1943-5606.0002605.

[38] Phoon K-K, Santoso A, Quek S-T. Probabilistic analysis of soil-water characteristic curves. J Geotech Geoenviron Eng 2010;136:445–55. https://doi.org/10.1061/(ASCE)GT.1943-5606.0000222.

[39] Dye HB, Houston SL, Welfert BD. Influence of unsaturated soil properties uncertainty on moisture flow modeling. Geotech Geol Eng 2011;29:161–9. https://doi.org/10.1007/s10706-009-9281-0.

[40] Likos WJ, Lu N, Godt JW. Hysteresis and uncertainty in soil water-retention curve parameters. J Geotech Geoenviron Eng 2014;140:04013050. https://doi.org/10.1061/(ASCE)GT.1943-5606.0001071.

[41] Yeh H-F, Huang T-T, Yang Y-S, Ke C-C. Influence of uncertainty of soil hydraulic parameters on stability of unsaturated slopes based on bayesian updating. Geofluids 2021;2021:6629969. https://doi.org/10.1155/2021/6629969.

[42] Field EH, Jacob KH. Monte-carlo simulation of the theoretical site response variability at Turkey flat, California, given the uncertainty in the geotechnically

derived input parameters. Earthq Spectra 1993;9:669–701. https://doi.org/10.1193/1.1585736.
[43] Sebastião PJ. The art of model fitting to experimental results. Eur J Phys 2013;35:15017. https://doi.org/10.1088/0143-0807/35/1/015017.
[44] Carsel RF, Parrish RS. Developing joint probability distributions of soil water retention characteristics. Water Resour Res 1988;24:755–69. https://doi.org/10.1029/WR024i005p00755.
[45] Phoon K-K, Kulhawy FH. Characterization of geotechnical variability. Can Geotech J 1999;36:612–24. https://doi.org/10.1139/t99-038.
[46] Phoon K-K, Kulhawy FH. Evaluation of geotechnical property variability. Can Geotech J 1999;36:625–39. https://doi.org/10.1139/t99-039.
[47] Taylor O-DS, Berry WW, Winters KE, Rowland WR, Antwine MD, Cunningham AL. Protocol for cohesionless sample preparation for physical experimentation. Geotech Test J 2017;40:20150220. https://doi.org/10.1520/GTJ20150220.
[48] Walshire L, Berry W, Taylor OD. Redesigned filter paper method: protocol and assessment using reconstituted samples. Geotech Test J 2020;44(2):237–54. https://doi.org/10.1520/GTJ20190420.
[49] Taylor O-DS, Martin KE. No Title 2017;9(606):87–B1.
[50] Martin KE, Taylor O-DS, Berry W, Rowland W. Near surface seismic signal response due to active fluid infiltration in partially saturated soil: laboratory analysis of observational phenomenon. Jt. Meet. Mil. Sens. Symp. Spec. Groups 2014:22–6.
[51] R Development Core Team. R A Language and environment for statistical computing. 2013.
[52] Venables WN, Ripley BD. Modern applied statistics with S. New York, NY: Springer New York; 2002. https://doi.org/10.1007/978-0-387-21706-2.
[53] Cullen A, Frey H. Probabilistic techniques in Exposure Assessment. First. New York, NY: Plenum Publishing Co; 1999.
[54] Efron B, Tibshirani R. An introduction to the bootstrap. First. Chapman & Hall; 1994.
[55] Delignette-Muller ML, Dutang C. Fitdistrplus : an R package for fitting distributions. J Stat Software 2015;64. https://doi.org/10.18637/jss.v064.i04.
[56] Taylor O-DS, Winters KE. Resonant Column behavior of unsaturated near-surface sands. PanAm unsaturated soils 2017. Reston, VA: American Society of Civil Engineers; 2018. p. 595–603. https://doi.org/10.1061/9780784481684.060.
[57] Taylor O-DS, Winters KE, Berry WW, Walshire LA, Kinnebrew PG. Near-surface soils: self-supported unconfined drained sand specimens. Can Geotech J 2018;56:307–19. https://doi.org/10.1139/cgj-2017-0261.
[58] Uyanık O. Estimation of the porosity of clay soils using seismic P- and S-wave velocities. J Appl Geophys 2019;170:103832. https://doi.org/10.1016/J.JAPPGEO.2019.103832.
[59] Suwal LP, Kuwano R. Statically and dynamically measured Poisson's ratio of granular soils on triaxial laboratory specimens. Geotech Test J 2013;36:20120108. https://doi.org/10.1520/GTJ20120108.
[60] Kumar J, Madhusudhan BN. Dynamic properties of sand from dry to fully saturated states. Géotechnique 2012;62:45–54. https://doi.org/10.1680/geot.10.P.042.
[61] Patel A, Ingale R, Bhanarkar KB. Effect of compaction states and the confining pressure on Poisson's ratio of stratified and non-stratified soils. Arabian J Sci Eng 2018;43:1983–99. https://doi.org/10.1007/s13369-017-2846-y.